remote sensing

MDPI

Article

Seven Years of SMOS Sea Surface Salinity at High Latitudes: Variability in Arctic and Sub-Arctic Regions

Estrella Olmedo [1,*], Carolina Gabarró [1], Verónica González-Gambau [1], Justino Martínez [1], Joaquim Ballabrera-Poy [1], Antonio Turiel [1], Marcos Portabella [1] and Severine Fournier [2] and Tong Lee [2]

1 Department of Physical Oceanography, Institute of Marine Sciences, CSIC & Barcelona Expert Center, Pg. Marítim 37–49, E-08003 Barcelona, Spain; cgabarro@icm.csic.es (C.G.); vgonzalez@icm.csic.es (V.G.-G.); justino@icm.csic.es (J.M.); joaquim@icm.csic.es (J.B.-P.); turiel@icm.csic.es (A.T.); portabella@icm.csic.es (M.P.)

2 Jet Propulsion Laboratory, California Institute of Technology, 4800 Oak Grove Drive, Pasadena, CA 91109, USA; Severine.Fournier@jpl.nasa.gov (S.F.); tlee@jpl.nasa.gov (T.L.)

* Correspondence: olmedo@icm.csic.es

Received: 14 September 2018; Accepted: 3 November 2018; Published: 8 November 2018

Abstract: This paper aims to present and assess the quality of seven years (2011–2017) of 25 km nine-day Soil Moisture and Ocean Salinity (SMOS) Sea Surface Salinity (SSS) objectively analyzed maps in the Arctic and sub-Arctic oceans (50°N–90°N). The SMOS SSS maps presented in this work are an improved version of the preliminary three-year dataset generated and freely distributed by the Barcelona Expert Center. In this new version, a time-dependent bias correction has been applied to mitigate the seasonal bias that affected the previous SSS maps. An extensive database of in situ data (Argo floats and thermosalinograph measurements) has been used for assessing the accuracy of this product. The standard deviation of the difference between the new SMOS SSS maps and Argo SSS ranges from 0.25 and 0.35. The major features of the inter-annual SSS variations observed by the thermosalinographs are also captured by the SMOS SSS maps. However, the validation in some regions of the Arctic Ocean has not been feasible because of the lack of in situ data. In those regions, qualitative comparisons with SSS provided by models and the remotely sensed SSS provided by Aquarius and SMAP have been performed. Despite the differences between SMOS and SMAP, both datasets show consistent SSS variations with respect to the model and the river discharge in situ data, but present a larger dynamic range than that of the model. This result suggests that, in those regions, the use of the remotely sensed SSS may help to improve the models.

Keywords: sea surface salinity; remote sensing; Arctic ocean; SMOS; Arctic rivers; data processing; quality assessment

1. Introduction

In recent years, the Arctic Ocean has been under significant changes as shown by numerous in situ and remotely sensed measurements. The temperature of the upper layer of the Arctic Ocean has been increasing and more solar heat has been absorbed by the increasing ice-free areas [1–3].

Latest observational and modeling studies have documented changes in the upper Arctic Ocean hydrography [4]. In particular, an increase of liquid freshwater content over both the Canadian Basin and the central Arctic Ocean has been observed. This increase of freshwater has been linked to an intensification in the large-scale anticyclonic winds as well as sea level pressure changes [5]. An increased Bering Strait freshwater import to the Arctic Ocean, a decreased Davis Strait export, and the enhanced net sea ice melt could play an important role in the observed freshwater trend [6].

Rivers are important sources of freshwater and heat to the Arctic Ocean and changes in the river runoff or temperature could have a strong impact on the Arctic system. An increment of the global mean annual temperature will produce an increase in the discharge of Arctic rivers [7,8].

The 2015 update of the Arctic Report Card alerts that, in 2014, the combined discharge of the eight largest Arctic rivers was 10% greater than their average discharge during the 1980–1989 period [9]. However, the impact of this increase of freshwater runoff on the Arctic ocean dynamics remains unknown due to the lack of available salinity measurements in the Arctic.

Unfortunately, the number of surface salinity measurements is very scarce at high latitudes, especially in the Arctic Ocean. In such context, the three L-band missions—the Soil Moisture and Ocean Salinity (SMOS) mission [10–12]; the Aquarius mission [13,14]; and Soil Moisture Active Passive (SMAP) observatory [15]—can provide an unprecedented source of salinity information over the Arctic Ocean, which can help to improve the models.

The retrieval of sea surface salinity (SSS) from microwave radiometric measurements is based on the emissivity of the ocean surface, which depends on the dielectric constant of sea water that is a function of temperature and salinity, and on the sea surface roughness. The SMOS radiometer operating frequency (1.43 GHz, in the L-band) provides good sensitivity of the ocean-surface brightness temperature (T_B) to SSS in the tropics and subtropics [16]. In cold waters, however, the sensitivity of the T_B to salinity decreases rapidly [17]. As shown in [18], such sensitivity drops from 0.5 K/psu to 0.3 K/psu, when SST decreases from 15 °C to 5 °C. Moreover, some undesired effects in SMOS T_B and to lesser extent in Aquarius and SMAP T_B measurements, such as the land–sea and ice–sea contaminations, and Radio Frequency Interference (RFI) [19] make the Arctic region one of the most challenging regions for SMOS SSS retrieval.

Some previous works assessed the quality of SMOS SSS at high latitudes. For example, in Köhler et al. [20] he authors performed a comparison of previous versions of SMOS (salinity maps computed from the L2OS v550) and Aquarius products with in situ measurements and models for the north Atlantic region, but they did not perform any comparison inside the Arctic Basin. Despite the large biases (mainly produced by land–sea and ice–sea contaminations) that affected the SMOS L2OS v550, in Matsuoka et al. [21] this product was used to develop an algorithm for identifying surface water sources in the southern Beaufort Sea by using Aqua/MODIS ocean color along with SMOS SSS L2. Recently, the potential and challenges of monitoring the Arctic Ocean SSS by using SMAP data have been demonstrated in [22].

A recently developed SSS retrieval algorithm [23] has noticeably improved the coverage of the global SMOS SSS leading to retrievals in some critical areas where no-valid or few salinity retrievals were available before (for example in the Mediterranean Sea [24,25]). The Barcelona Expert Center (BEC) team used this methodology for the generation of three-year time series of SMOS SSS at high latitudes. In [26], a comparison of these SMOS SSS maps and three other SSS products provided by Aquarius with in situ data is performed. The authors concluded that SMOS SSS maps are consistent with ship and CORA5.0 data, although they also pointed out that the sea ice mask should be improved.

In this work, we generate seven years of SMOS SSS maps at high northern latitudes (beyond 50°N) by using the methodology described in [23]. Additionally, we improve the methodology in terms of the seasonal bias. The objectives of this work are the following: (i) to present seven-year time series of this new SMOS SSS product at high northern latitudes; (ii) to assess the quality of these new SMOS SSS maps at high latitudes by comparing them to different sources of in situ data; (iii) to compare the SMOS SSS with other available products in this region (model and other remotely sensed SSS products); and (iv) to show the potential of SMOS SSS to capture the SSS variability in the Arctic region.

The paper is structured as follows: In Section 2, we describe the different datasets that are used. In Section 3, the methodology used for the generation of the SMOS salinity maps is briefly presented. The assessment of the SMOS salinity maps is presented in Section 4. Variations of SSS shown by SMOS, Aquarius, SMAP and the model outputs from TOPAZ close to the mouth of the major Arctic rivers are shown in Section 5. A final discussion is provided in Section 6.

2. Datasets

2.1. SMOS Brightness Temperatures: Level 1B Product

The input data for the computation of the SMOS SSS maps are the Level 1 Brightness Temperature product (L1B v620). This product consists of the Fourier components of brightness temperatures in the antenna reference frame. The latency of the products is 6–8 h. The L1B T_B product is distributed by the European Space Agency (ESA) and is freely available at https://earth.esa.int/web/guest/-/how-to-obtain-data-7329.

2.2. Argo Salinity

We use Argo salinity [27] in Section 3 for the characterization of the SMOS SSS bias and for the generation of a time-dependent bias correction. After that, Argo data are also compared with the resulting SMOS products in Section 4.2.

We consider the uppermost salinity measurement provided by the Argo profiles (hereafter, Argo SSS) to be compared with the nine-day SMOS SSS maps. Thus, for every SMOS SSS nine-day map, the available Argo SSS during these nine days are compared with the corresponding fields of the SMOS SSS map. The cut-off depth for Argo profiles is taken at 10 m but no measurements shallower than 0.5 m are used due to the formation of bubbles and foam. In the case of SOLO and PROVOR Argo floats, only the data deeper than 5 m below the surface are used because their Conductivity, Temperature and Depth (CTD) probes stop pumping water at around 5 m below the surface. Profiles from BioArgo and those included in the greylist (i.e., floats which may have problems with one or more sensors) are discarded. In addition, we use World Ocean Atlas (WOA) 2013 as an indicator: Argo float profiles with anomalies larger than 10 °C in temperature or 5 PSU in salinity when compared to WOA are discarded. Only profiles having temperature close to surface between −2.5 and 40 °C and salinity between 2 and 41 PSU are used. In Figure 1 (top-left), the number of Argo SSS and their spatial distribution for the period of study is represented.

2.3. TARA Salinity

The Tara Polar Circle Expedition dataset (hereafter, TARA SSS) [28] is used to validate the SMOS nine-day maps in the Arctic. This campaign took place in the Arctic Ocean from June to October 2013, and a thermosalinograph (TSG) Seabird SB45 and a temperature sensor (SBE38) recorded sea surface temperature and salinity at 3 m depth during the whole cruise. Since TARA salinity data present a large range of spatial variability in the Arctic Ocean (≈26 to 35), they are a very valuable source for assessing the annual SSS reference used for the generation of the SMOS SSS product.

The collocation strategy between satellite and TARA SSS is the following: for a given time instant t_0 at which a value of TARA SSS was acquired, that value is compared with the nine-day SMOS SSS map centered around t_0. All the TARA SSS data that cross a single SMOS cell (25 × 25 km) are averaged and the resulting mean value is the one that is compared with the SMOS SSS. In Figure 1 (top-right), the TARA SSS data measured in the expedition are represented.

2.4. TSG Salinity Data

We use 86 transects provided by Copernicus (hereafter, TSG SSS) for assessing the SMOS SSS. These data are freely available on http://marine.copernicus.eu/services-portfolio/access-to-products/ and are labeled as INSITU_ARC_NRT_OBSERVATIONS_013_031. In Figure 1 (bottom-left), the locations of the measurements are shown. The collocation strategy between SMOS and TSG SSS is the same as that of SMOS and TARA. Only TSG SSS data flagged as "good quality" have been used.

Measurements deeper than 10 m are discarded. In Section 4.3, this dataset is used as an independent reference for the SMOS SSS validation.

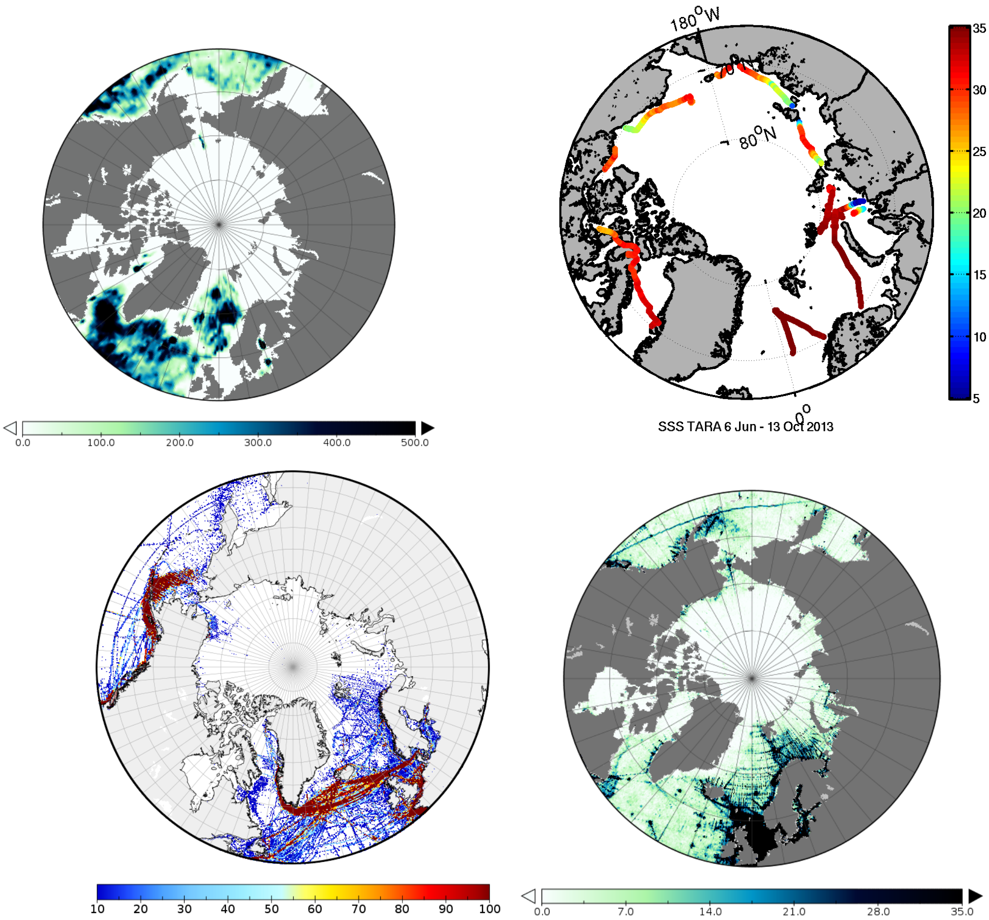

Figure 1. Number of measurements provided by Argo floats in the period of study 2011–2017 (**top-left**); salinity values (using the practical salinity scale) provided in the TARA campaign (**top-right**); number of SSS measurements provided by the TSG that have been used in this study for validation (**bottom-left**); and number of in situ measurements used in the computation of annual SSS climatology WOA (**bottom-right**).

2.5. TOPAZ Salinity

In Section 5, for those regions where no in situ measurements are available, we compare the variability shown by SMOS SSS with the one captured by TOPAZ (Towards an Operational Prediction system for the North Atlantic European coastal Zones) SSS. The TOPAZ Arctic Prediction system consists of a coupled ocean sea ice data assimilation system (Ensemble Kalman filter) for the North Atlantic and the Arctic Ocean using the Hybrid Coordinate Ocean Model (HYCOM [29]). Satellite and in situ observations (including Argo floats) are assimilated. The observations assimilated in the system are satellite-derived sea level anomaly, SST, sea-ice concentrations from AMSR-E, sea-ice drift products from CERSAT and Coriolis, and in situ temperature and salinity profiles [30]. Since no SMOS SSS can be derived over sea ice, only grid points with sea ice fraction lower than 30% have been used when comparing TOPAZ and SMOS SSS. It is important to mention that TOPAZ relaxes SSS to seasonal climatology [31]. This has implications for the dynamic range of SSS from TOPAZ in regions without sufficient in situ salinity measurements to constrain the model during the data assimilation. Data since October 2011 are available at the Copernicus web page http://www.copernicus.eu/.

2.6. Aquarius SSS L3 Maps

The Aquarius/SAC-D mission dataset consists of weekly gridded products of L-band (frequency 1.4 GHz) radiometer SSS [32]. This product contains the average SSS retrieved from all the three beams of Aquarius. Data are then gridded to the Equal-Area Scalable Earth version 2.0 grid [33], with a cell resolution of 36 km. Version 5 of Aquarius L3 Weekly Polar-Gridded Sea Surface Salinity utilizes Version 4 of the Level-2 Aquarius SSS as input data. The product is distributed by the National Snow and Ice Data Center (NSIDC, http://nsidc.org/data/aq3_sss).

2.7. SMAP SSS L3 Maps

We use the level-3 SMAP SSS version-4 dataset produced by the Jet Propulsion Laboratory [34] at 0.25° horizontal resolution and eight-day running average time window from 31 March 2015 to 31 December 2017. The horizontal resolution of SMAP SSS is 40 km. Data are then gridded to the Equal-Area Scalable Earth version 2.0 grid [33], with a cell resolution of 36 km. The data are available on the PO.DAAC website (https://podaac.jpl.nasa.gov/dataset/SMAP_JPL_L3_SSS_CAP_8DAY-RUNNINGMEAN_V4).

2.8. River Discharge In Situ Measurements

Discharge data, provided by river gauge measurements made under the Arctic Great Rivers project (http://www.arcticgreatrivers.org/) from 2011 to 2017, are used in Section 5 for completing the description of the inter and intra annual variability observed by SMOS SSS close to the major Arctic river mouths.

3. Methodology Used for the SMOS SSS Product Generation

Seven years (2011–2017) of the SMOS L1B T_B data product (v620), provided by the ESA, are processed to generate salinity maps at high latitudes (from 50°N to 90°N).

The galactic [35], sun glint [36] and surface roughness [37] contributions are corrected using auxiliary information provided by ECMWF [38], similar to what is done in the official ESA SMOS L2 SSS products. The dielectric constant model proposed by Meissner and Wentz (M&W) [39] is used instead of the model defined by Klein and Swift (K&S) [40], which is used in the official SMOS Ocean Salinity Level 2 product. The work presented in [41] shows that, when analyzing SSS from Aquarius, differences between M&W and K&S are small at low and mid latitudes, but they increase at high latitudes, i.e., in cold waters. The authors concluded that, for very cold waters (colder than 3 °C), retrieved salinities using M&W model are significantly closer to in situ floats measurements than those retrieved using K&S.

The T_B measurements are geo-referenced using a 25-km resolution Equal-Area Scalable Earth (EASE) North Pole grid [42]. To account for the SMOS residual spatial and temporal systematic errors, the SSS retrieval methodology presented in [23] is used. This methodology introduces important changes with respect to the standard processing [16,43] used in the ESA SMOS L2OS processor:

(a) Individual retrievals: The retrieval follows a non-Bayesian scheme, that is, for each SMOS T_B a single value of SSS is retrieved.

(b) Characterization of the systematic errors: All the SSS retrieved under the same acquisition conditions, i.e., the same geographical location, incidence and azimuth angles and satellite overpass direction (ascending/descending). throughout this seven-year period are accumulated in a SSS distribution. The systematic error associated to each acquisition condition is estimated by computing the central estimator of the corresponding SSS distributions. We use the mode of the distribution as the central estimator, i.e., as the SMOS climatological value for each specific acquisition condition. In this aspect, a relevant difference with respect to the official SMOS L2OS processor is that the T_B used for the ESA SMOS L2OS SSS retrieval are previously corrected by Ocean Target Transformation (OTT) [44]. The OTT is computed as the mean of the difference between the measured and modeled T_Bs (applying the Geophysical Forward Model) at a particularly stable region of the ocean. We do not apply an OTT since systematic errors are already accounted for, point by point, with the new methodology.

(c) Filtering criteria: The statistical properties of those SSS distributions are also used for filtering the non-accurate measurements. Two types of filters are applied to remove questionable values and outliers in the SSS retrievals: (i) all the SSS belonging to distributions having a large standard deviation (std larger than 10), defined by too few measurements (less than 100), or with a large skewness (larger than 1 in absolute value) or kurtosis (lower than 2) are all excluded (i.e., the distribution is marked as "bad" distribution, and all its salinities are discarded); and (ii) an additional outlier criterion is applied to the remaining retrieval values by further excluding any value that is farther than 10 (in absolute value) from the SMOS climatological value (see more details in [23]).

(d) Computation of SMOS anomalies: The SMOS-debiased SSS anomalies are computed by subtracting to each individually retrieved SSS value (corresponding to a specific acquisition condition) the corresponding SMOS climatological value (computed as explained in (b)), thus effectively removing local biases, especially those produced by the land–sea (or ice–sea) contamination and permanent RFIs.

(e) Computation of SMOS SSS: In [23], the SMOS SSS are generated by adding an annual SSS reference (annual WOA SSS, [45]) to the SMOS anomalies. This is an issue for the SMOS SSS values of the Arctic Ocean, since there are many zones in the Arctic with very few measurements of SSS (as shown in the bottom-right plot of Figure 1), and any reference could provide non-accurate SSS values there. For this reason, before generating the seven years of SMOS SSS, we analyze two test datasets by using two annual references: WOA; and the Polar science center Hydrographic annual Climatology (PHC) (version 3) [46] which is the usual reference for Arctic regions. We assess the quality of these two datasets by comparing the resulting SMOS SSS products—the SMOS SSS computed from WOA annual reference (SMOS woa) and SMOS SSS computed from PHC (SMOS phc)—with TARA SSS. In Section 4.1, a full discussion of this assessment is given. The conclusions of these comparisons are summarized in Figure 2. SMOS SSS has lower RMS with respect to TARA SSS than the corresponding annual references used for its generation (i.e., the blue and red lines are below the green and black lines, respectively, except in Buffin Bay where the SMOS-PHC has slightly larger RMS than the PHC product). The actual RMS values, together with the bias and standard deviation values, can be found in Table 1. However, many regions in the Arctic Ocean present large RMS values. These regions correspond to the areas where few or no in situ data were taken into account in the generation of the annual reference. In Section 4.1, we describe this analysis in more detail. Since both references provide similar results (WOA is slightly better), we use WOA for the generation of SMOS SSS product to be coherent with the global SMOS SSS product distributed by BEC.

(f) Objectively analyzed maps: Objectively analyzed nine-day SSS maps at 25-km resolution are generated daily. In [23], the same correlation radii used for the computation of WOA products were proposed for the generation of the SMOS SSS products: 321 km, 267 km, and 175 km (see [45]). These correlation radii do not seem to be the most appropriate for describing the dynamics in the Arctic region [47]. For this reason, we assess the impact on SSS quality of using different correlation radii, by means of the following experiment:

- We consider a finite set of candidates for the first correlation radius, R_1: 175 km, 200 km, 225 km, 250 km, 275 km, 300 km, and 325 km.

- For each one of the previous values, we consider the second R_2 and third R_3 radii of convergence such that:

$$R_2 = R_1 * \gamma \tag{1}$$
$$R_3 = R_2 * \gamma \tag{2}$$

  with γ taking each one of the following values: $\gamma = 0.3, 0.4, 0.5, 0.6, 0.7, 0.8$.
- For each set of three convergence radii computed as before, we generate seven months of SMOS nine-day SSS maps: from the 1 April to the 9 November of 2013, one map every five days.
- We apply the time-bias correction proposed in [23], by removing the (spatial) mean anomaly between each SMOS SSS map and the annual WOA SSS.
- We compare the resulting SMOS SSS with Argo SSS. We use as a metric the global RMS of the difference between SMOS and Argo SSS, averaging the seven months for each one of the previous choices of R_1 and γ.

The configuration which provides the lowest error ($RMS \approx 0.25$) is the one with $R_1 = 325$ km and $\gamma = 0.8$, which is the closest one to the configuration proposed in [23]: 321 km, 267 km and 175 km. Notice that the global L3 SMOS SSS maps distributed by BEC (http://bec.icm.csic.es/ocean-experimental-dataset-global/) use a set of smaller correlation radii (175 km, 125 km and 75 km) for better describing the mesoscale. The results raised from this experiment suggest that, at high latitudes, the larger is the correlation radii, the larger is the smoothing effect, and therefore the lower is the noise. This is probably because individual SMOS SSS retrievals at high latitudes are noisier than in other regions of the globe. In other words, the generation of SMOS SSS maps with smaller correlation radii and the same level of noise as in the case of the global SSS maps requires SMOS SSS retrievals less noisy. In this sense, improvements at T_B level as the ones introduced in [48] and assessed at salinity level in [49,50] are providing promising results in terms of noise reduction in the SSS retrievals. The application of this technique will probably help to retrieve more accurate SSS in those regions and therefore to generate SMOS SSS maps with smaller correlation radii (more appropriate to capture the dynamics of this region).

(g) Mitigation of the seasonal bias: An additional time-dependent bias correction is needed to mitigate the effect of seasonal and other time-dependent biases which affect the SMOS T_B ([19]). In [23], the authors proposed subtracting the global mean of the SMOS SSS anomaly for each nine-day map. This assumption is appropriate for global SSS maps, as it implies that the total content of salt remains constant in time. However, the application of this hypothesis regionally, in particular at high latitudes, produces seasonal biases. In other words, there are net exchanges of salinity across region boundaries. In a recent study [25], a multivariate analysis is used to characterize and mitigate the time-dependent bias in the SMOS SSS maps in the Mediterranean Sea. In this work, we include a simpler time-dependent bias correction:

- We consider the Argo SSS available for the same nine-day period used in the generation of the nine-day SMOS SSS maps.
- We compute the median of the differences between the collocated SMOS SSS fields and the Argo SSS.
- We subtract this median from each nine-day SMOS SSS map.

Figure 3 shows the time-dependent correction resulting from this procedure, which has been applied to each map.

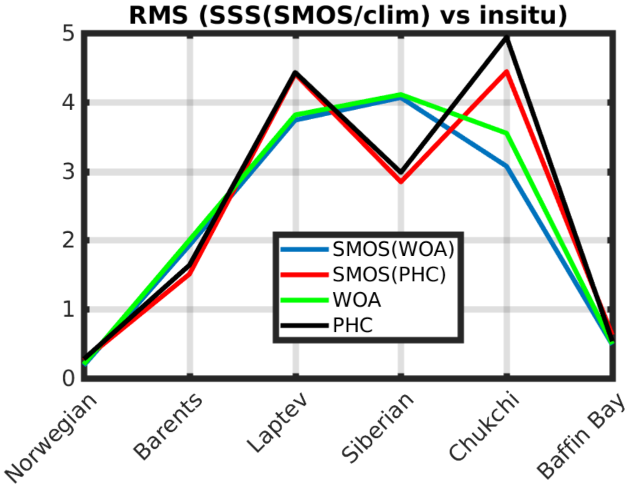

Figure 2. Assessment of the impact associated to the choice of the annual climatology in the SMOS SSS product generation. The blue line corresponds to the root mean square (RMS) of the differences between SMOS SSS derived with WOA annual mean and the TARA SSS; the red line corresponds to the RMS of the differences between SMOS SSS derived with PHC annual mean and TARA SSS; and the green (black) line represents the RMS differences between WOA (PHC) SSS and TARA SSS.

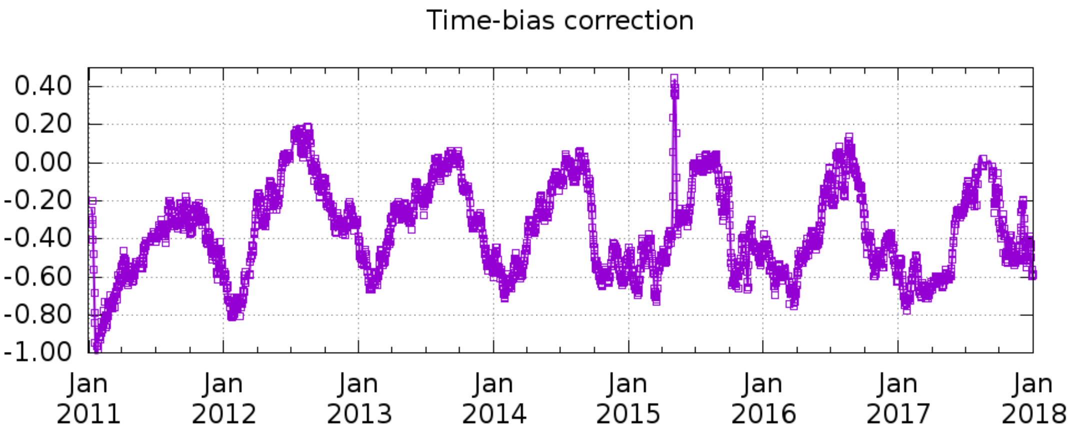

Figure 3. Time-bias correction applied to the nine-day SMOS SSS L3 maps. During 1–10 January 2011, SMOS provided degraded acquisitions due to a problem in the physical temperatures acquisition (reported in https://earth.esa.int/c/document_library/get_file?folderId=118493&name=DLFE-5407.pdf). The reason for the jump at the end of April 2015 is still under study, but is probably related to several degraded orbits that were reported in the data quality report (available on https://earth.esa.int/documents/10174/1785702/SMOS_Public_Monthly_Report_April_2015).

Table 1. Statistics in the comparison of SMOS SSS with TARA SSS.

Arctic Region	SMOS woa			WOA			SMOS phc			PHC		
	Mean	Std	RMS	Mean	Std	RMS	Mean	Std	RMS	Mean	Std	RMS
Norwegian sea	0.11	0.15	0.18	−0.06	0.19	0.20	−0.18	0.19	0.26	−0.13	0.24	0.28
Baffin Bay	0.16	0.46	0.49	0.04	0.49	0.50	0.29	0.55	0.63	0.17	0.51	0.54
Chukchi region	2.16	2.18	3.07	2.74	2.26	3.55	3.46	2.79	4.44	4.02	2.87	4.94
Barents sea	−1.35	1.37	1.93	−1.22	1.58	2.00	−0.86	1.24	1.51	−0.73	1.46	1.64
Laptev sea	1.37	3.48	3.74	1.78	3.37	3.81	1.46	4.16	4.41	1.87	4.02	4.43
Siberian region	−3.20	2.50	4.06	−2.88	2.93	4.11	−1.54	2.39	2.84	−1.21	2.72	2.98

4. Quality Assessment of the SMOS SSS Data

4.1. Comparison with TARA SSS: Impact Analysis of the SSS Annual Reference

As explained in Section 3, the computation of the final value of the SMOS SSS maps depends on the annual SSS reference. In this section, we compare with TARA SSS two SMOS SSS products which use different annual SSS references: the SMOS SSS using WOA annual reference (SMOS woa) and SMOS SSS using PHC (SMOS phc).

The validation against TARA SSS is done by separating the transects per different seas, for a better understanding of the regional quality of the SMOS SSS product. We divide the whole dataset into six regions: Norwegian Sea, Barents Sea, Laptev Sea, East Siberian Sea, Chukchi Sea and Baffin Bay.

Figure 4 (right) shows differences of TARA SSS and SMOS woa and SMOS phc SSS. To keep the figure readable, the WOA and PHC climatological values have been excluded from the right plots. Note that, although the differences of SMOS and in situ are lower than those of the corresponding climatologies and in situ, it is clear that, when the climatological values largely deviate from the in situ values (e.g., in the Chuckchi Sea, up to 8 PSU deviations are observed), the SMOS product also shows large deviations, therefore indicating that the annual climatology plays an important role in the quality of the SMOS-derived products. Let us comment in more detail the statistics in the different regions.

The comparison for the Norwegian Sea (June 2013) is shown in the first row of Figure 4. The RMS between SMOS and TARA in that transect is 0.18 (for SMOS woa) and 0.26 (for SMOS phc) (see Table 1). In the Norwegian Sea region, the annual WOA SSS was generated with a lot of in situ measurements (as shown in Figure 1 (bottom-right)). Thus, proper SSS values for the reference are expected.

The bottom-right plot of Figure 1 shows also some in situ measurements in the Greenland coast and in the Beaufort Sea. The Tara Polar circle Expedition crossed the Baffin Bay in October 2013. Plots in the second row of Figure 4 show the comparison between TARA and SMOS measurements with a mean RMS of 0.49 for SMOS woa and 0.63 for SMOS phc.

In September 2013, the expedition arrived to the Chukchi region. Large errors of SMOS measurements with respect to TARA are observed in the Canadian coast (see the plots in the third row of Figure 4) with a RMS of 3.07 and 4.44 for SMOS woa and SMOS phc respectively (Table 1). Although some in situ data are available for the computation of the annual reference (bottom-right plot of Figure 1), they may not be sufficient for generating an accurate annual reference in this region, which is affected by a large dynamic range of salinity due to the fresh water coming from the Mackenzie River.

The other three regions that we analyze (Barents, Laptev and Siberian Seas) correspond to regions where no or very few in situ data are available for the computation of the WOA (see bottom-right plot of Figure 1). In these three cases, the differences observed between SMOS and TARA SSS are larger than what is expected, with RMS greater than 1 psu in all cases. Neither WOA nor PHC seems to provide a proper annual reference for the computation of SMOS SSS. Let us comment each one of the three regions separately:

The comparison in the Barents Sea (July 2013) is shown in the forth row of Figure 4. The differences between TARA and SMOS measurements increase when the ship goes to the Kara Sea region and near the Yenesey River mouth, where SMOS always measures fresher waters than TARA. The Ob and Yenesey River plumes affect that region. This could explain part of the negative differences observed: while SMOS measures the salinity in the top cm of the ocean, TARA measures at 3 m depth. The stratification at these epochs of the year is usually strong, so, some negative differences are expected [51]. Another possible explanation for these differences is that these regions are typically affected by RFI. Although the methodology described in Section 3 aims to mitigate permanent effects of RFI, some residual RFI contamination may affect the SSS retrievals in this region. On the other hand, although differences of few psu are observed between satellite and in situ (1.93 in the case of SMOS woa and 1.51 in the case of SMOS phc), SMOS follows the full range of SSS observed by TARA in this region (also goes from 35 to 25 psu with both annual SSS references).

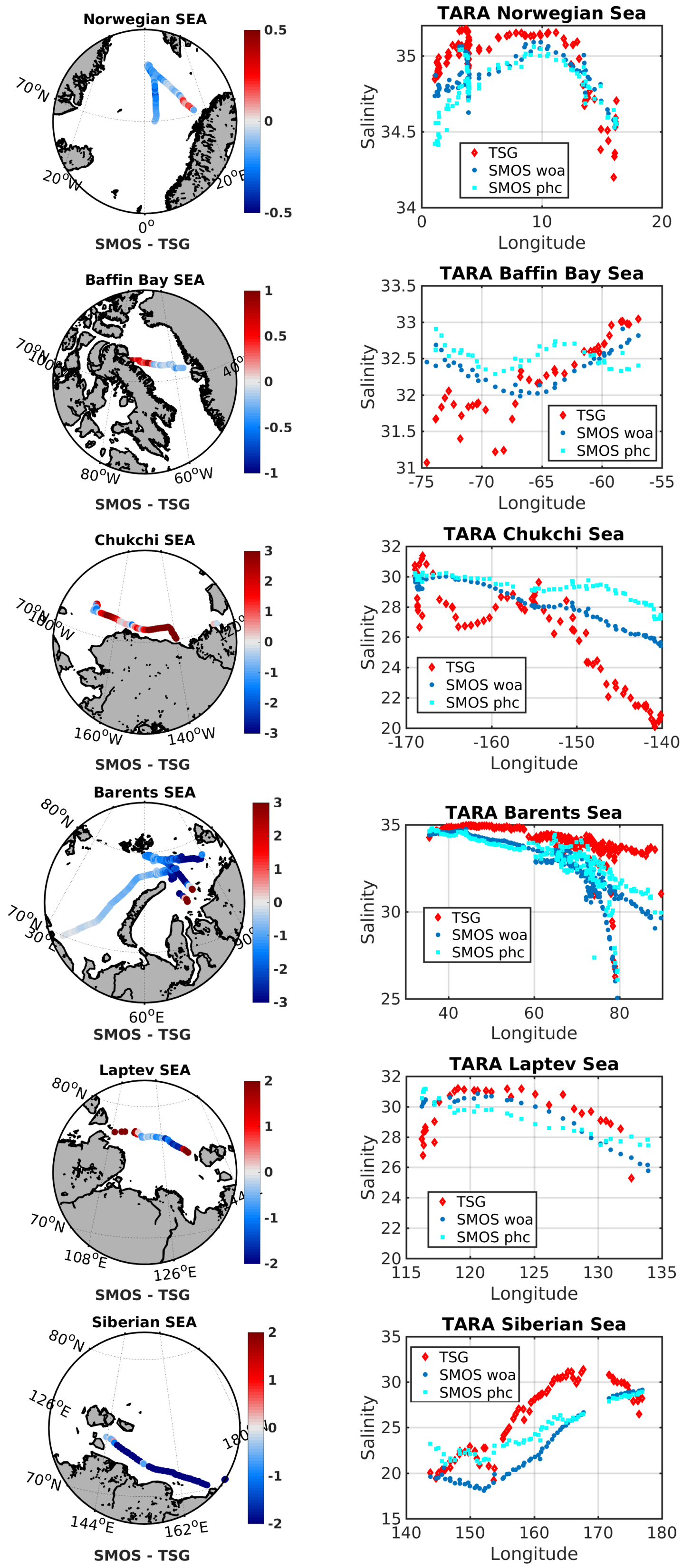

Figure 4. (**Left**) Difference between SMOS SSS and TARA SSS. (**right**) TARA, SMOS woa and SMOS phc SSS as function of the longitude. From top to bottom: Norwegian Sea in June 2013; Baffin Bay in October 2013; Chukchi Sea in September 2013; Barents Sea in July 2013; Laptev Sea in August 2013; and Siberian Sea in August 2013.

The expedition crossed Laptev Sea and Siberian region in August 2013. In both comparisons (see plots in the sixth and fifth rows, respectively, of Figure 4), as in the Barents Sea, SMOS measured fresher than TARA. In the Laptev Sea, although the mean RMS is about 3.74 for SMOS woa and 4.41 for SMOS phc, SMOS recovers the same SSS range as TARA (from 32 to 26 psu). In the Siberian region, the differences between satellite and TARA result in a RMS of 4.06 for SMOS woa and 2.84 for SMOS phc. Part of these negative differences can be explained because of the proximity to the coast and the river discharges (as occurs close to the Yenesey River mouth). Despite these large differences in the value of SSS, the dynamical range of SMOS SSS is similar to the one of TARA: TARA goes from 20 to 32 psu; SMOS woa from 18 to 30 psu; and SMOS phc from 20 to 30 psu. To better illustrate this, we include in Table 2 the correlation between the SMOS SSS products and TARA over the analyzed regions (similar values are obtained for the corresponding annual climatologies, not included). Correlation between SMOS phc and TARA in the Baffin Bay and Laptev Sea is very low (even negative). However, in the case of SMOS woa, despite the large biases between SMOS and TARA SSS, the correlation between both datasets is higher than 0.7 in most of the regions. This means that the major features of the spatial salinity gradients captured by the SMOS SSS in those regions are coherent with the ones captured by TARA SSS.

Figure 2 summarizes the main results discussed in this section. The conclusions are that there are some regions in the Arctic Ocean where no annual SSS reference is good enough and more efforts should be dedicated to the generation of a better reference. Since both analyzed references provide similar results in terms of RMS, but SMOS woa provides better correlation with TARA, we select WOA to develop the SMOS SSS products. This choice is also coherent with the annual reference selected for the global SMOS SSS products distributed at the BEC.

Table 2. Correlation of SMOS SSS with respect to TARA SSS.

	Norwegian Sea	Baffin Bay	Chukchi Region	Barents Sea	Laptev Sea	Siberian Region
SMOS woa	0.73	0.51	0.91	0.88	0.68	0.80
SMOS phc	0.56	−0.20	0.86	0.91	0.28	0.81

4.2. Comparison with Argo SSS

In this section, a statistical comparison between the nine-day SMOS SSS products and salinity provided by Argo floats (see Section 2.2) is presented. Since we use Argo floats for performing the time-dependent bias correction (see Section 3), this dataset is not an independent source of SSS data to be used for assessing the global mean of the product. However, this comparison is used to assess the residual spatial biases and the uncertainty (standard deviation of the differences SMOS-Argo SSS) of the SMOS SSS product.

In Figure 5, the mean of the differences between SMOS and Argo SSS during 2011–2017 are displayed (left), as well as the standard deviation of these differences (right). Large differences are observed in the Baffin Bay, the Labrador Sea and the eastern coast of Greenland (Greenland sea and Fram Strait). A possible factor contributing to these differences is the high-frequency and small-scale variability of SSS associated with the currents and the differences in temporal and spatial samplings between SMOS and the Argo SSS. SMOS maps are based on nine-day averages while Argo SSS represents instantaneous salinity values. Besides, SMOS SSS provides spatial average within a 40-km footprint, further smoothed by the Objective Analysis large correlation radii (see Section 3), while in situ data are instantaneous and point-wise measurements. The differences caused by these effects could be substantial if there are significant sub-footprint variability [51].

The northern coast of Alaska also presents large discrepancies between SMOS and Argo SSS. This region is strongly stratified, and the mixed layer is typically thinner than 3 m in this region. This implies also a limitation in the comparison of SMOS with Argo data since SMOS is measuring the first cm depth and Argo SSS are typically provided at some meters depth.

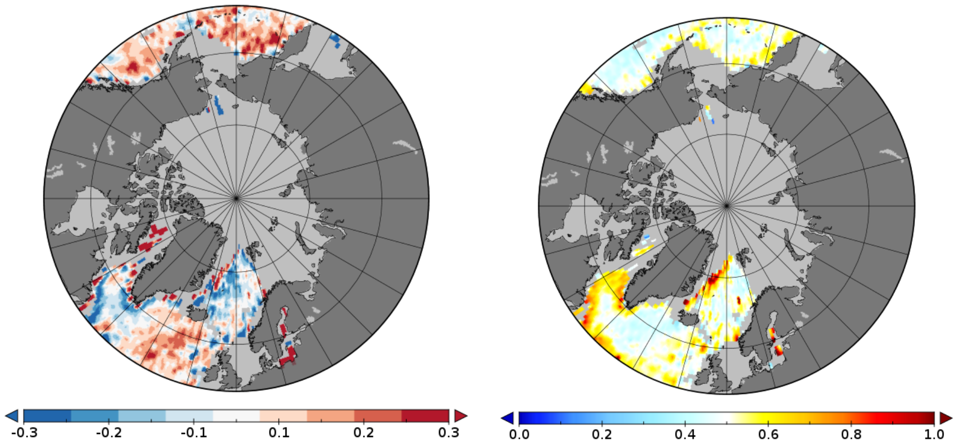

Figure 5. Spatial distributions of the differences between SMOS and Argo SSS: (**Left**) the mean of SMOS-Argo SSS; and (**Right**) the std of the difference.

Figure 6 shows temporal evolution of the the standard deviation of the differences SMOS-Argo SSS (top) and the number of collocations used in the statistics (bottom), such that, for a given time t_0 (x-axis), the point represents the std of the differences between SMOS and Argo SSS and the number of collocations, respectively, for all the collocations available with t_0 the first day of the nine-day period. We do not show the time evolution of the mean difference of SMOS and Argo SSS because, by definition (see Section 3), it is zero since the seasonal bias that was present in the previous version of this product has been mitigated. Large std values are observed in autumn 2012. The causes for such large std values (whether geophysical or instrumental) are currently being investigated. Our preliminary hypothesis indicates that they are due to a strong RFI episode. The std of the differences between SMOS and Argo SSS is between 0.24 and 0.35.

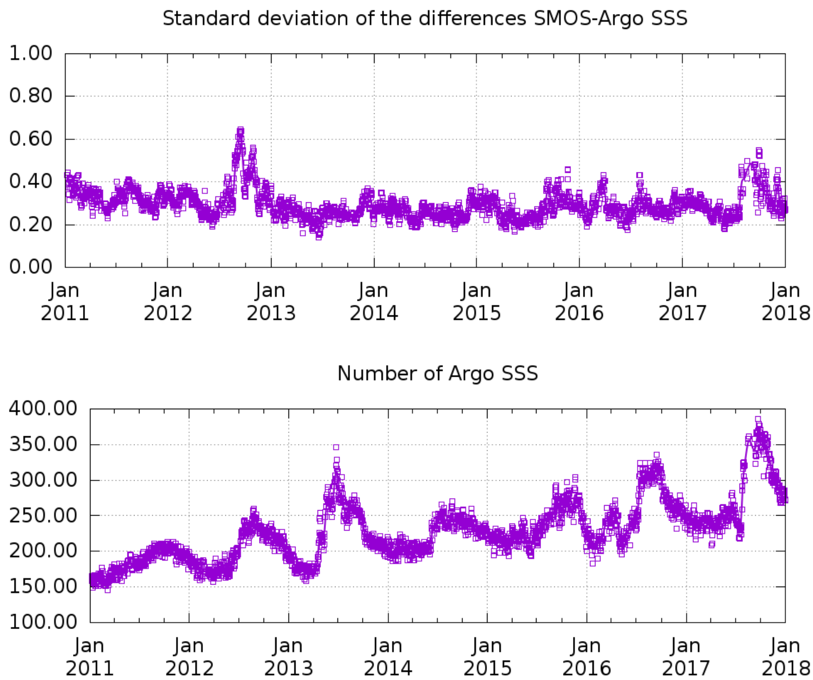

Figure 6. Time evolution of the standard deviation of the differences between SMOS and Argo SSS (**top**); and the number of measurements used in the comparison (**bottom**). The statistics are computed for data above 50°N. Every SMOS nine-day map is compared with the Argo SSS available for the same nine-day period.

4.3. Comparison with TSG Data from Copernicus

In this section, we compare SMOS SSS with SSS provided by 86 TSG transects distributed by Copernicus. The objective is to show that both SSS sources agree on the major features of the inter annual SSS dynamics, despite the different spatial and temporal resolutions of TSG and SMOS data. The statistics of the differences between SMOS and TSG SSS in several regions are provided in Table 3. In general, SMOS SSS has a positive bias with respect to TSG SSS. More detailed discussions of the results shown in Table 3 are provided below.

Table 3. Regional analysis on the differences between TSG and SMOS SSS (SMOS-TSG). Regional statistics of differences between SMOS and ARGO are also included.

Region	Latitude Range	Longitude Rage	SMOS-TSG			SMOS-ARGO		
			Meas	Mean	Std	Meas	Mean	Std
Denmark Strait	60N–65N	40W–25W	2322	0.22	0.28	25,153	0.02	0.21
North Atlantic	50N–60N	50W–20W	8028	0.19	0.45	102,575	0.01	0.35
Norwegian Sea	60N–70N	10W–5E	4587	0.02	0.67	33,841	−0.05	0.31
Northern Sea	55N–60N	0E–5E	53,366	0.16	0.99	0	-	-
Gulf of Alaska	55N–60N	175W–125W	604	0.26	0.72	14,841	0.09	0.27
Chuckchi Sea	70N–75N	170W–145W	315	0.01	1.42	1751	−0.99	0.37
Labrador Sea	55N–60N	55W–45W	737	0.14	0.71	33,711	−0.07	0.29
Baffin Bay	60N–65N	65W–55W	278	0.89	0.62	5919	−0.02	0.41

In the North Atlantic and Denmark Strait, the biases are 0.22 and 0.19, respectively, and the standard deviations are 0.28 and 0.45, respectively. These values of the standard deviation are in the expected range of error if we compare with the ones provided in the comparison with Argo (see Table 3). In the other regions, the standard deviations are larger than the standard deviations resulting from the comparison with Argo. Part of the increase in the standard deviation can be explained because the TSG SSS data reach more coastal regions than the Argo data do. Typically, these coastal regions are affected by complex circulation dynamics that could form filaments and mesoscale and submesoscale structures with strong SSS gradients and fast dynamics that cannot be resolved by SMOS, particularly after applying objective analysis. In those regions, we typically observe that the TSG captures strong SSS gradients with differences between consecutive coastal pixels greater than several PSU.

In Figures 7 and 8, TSG and collocated SMOS SSS are shown for 2013 and 2015, and 2012 and 2014, respectively, over two regions: the Norwegian and Northern Seas (Figure 7) and the Baffin Bay and the Labrador Sea (Figure 8). In both figures, near the coast, the TSG captures strong SSS gradients displaying consecutive salinity values of one lower than 33.5 and the next salinities saltier than 35 (in the Norwegian coast) and lower than 32 and saltier than 34 (in the Greenland coast). These strong SSS gradients are marked with red lines in Figures 7 and 8. Objectively analyzed SMOS SSS cannot fully capture these dynamics among other reasons because objectively analyzed maps are produced using correlation radii of 325–175 km. However, both sources of SSS are in good agreement regarding the major features of the spatial SSS gradients and the inter annual variability. For example, in 2013, TSG SSS captures a freshening in the southern part of the Norwegian Peninsula which spreads through the Northern Sea. SMOS SSS also shows fresher SSS in 2013 than in 2015 and it captures the spreading of the fresh water towards the Northern Sea (green circles in Figure 7). On the southern coast of Baffin Island, both sources of salinities agree on capturing fresher SSS in 2012 than in 2014 (green circles in Figure 8).

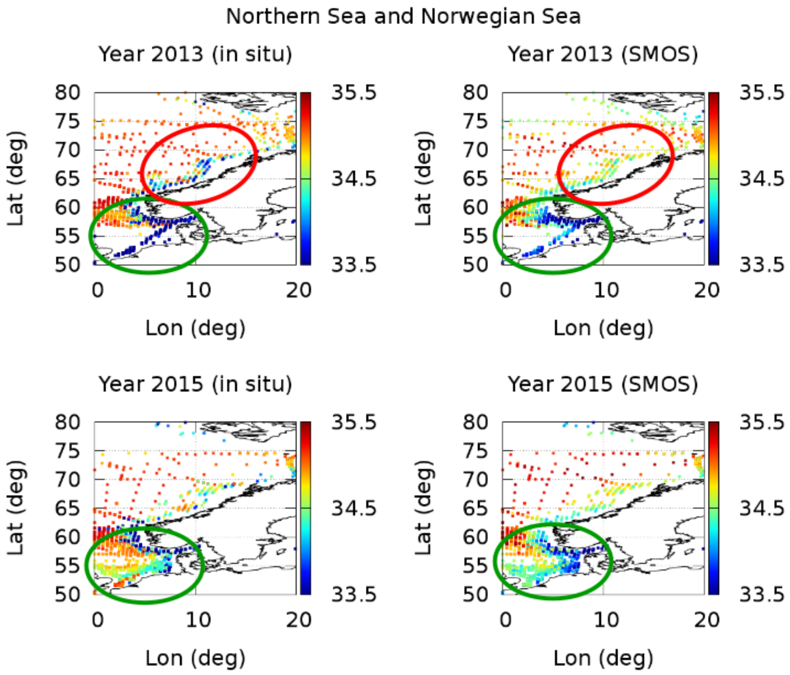

Figure 7. TSG (**left column**) and SMOS (**right column**) SSS in the Northern and Norwegian Seas for 2013 (**top**) and 2015 (**bottom**).

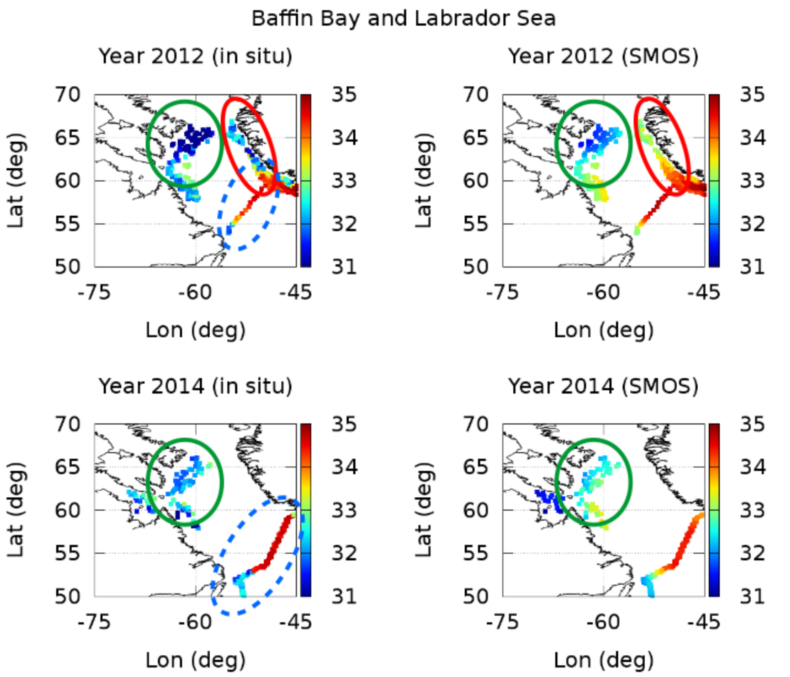

Figure 8. TSG (**left column**) and SMOS (**right column**) SSS in the Baffin Bay and Labrador Sea for 2012 (**top**) and 2014 (**bottom**).

To better analyze the inter annual variability, we study three routinely annual-performed transects: (i) one horizontal transect in the Gulf of Alaska around 58°N (first and second plots of Figure 9); (ii) one vertical transect in the Baffin Bay with longitude fixed around 79°W and latitudes in a range of 57°N and 67°N (third and forth plots of Figure 9); and (iii) one diagonal transect in the Labrador Sea (encircle with a dashed blue line in Figure 8) with a latitude range from 50°N to 60°N; and longitude range from 55°W to 50°W (fifth and sixth plots of Figure 9).

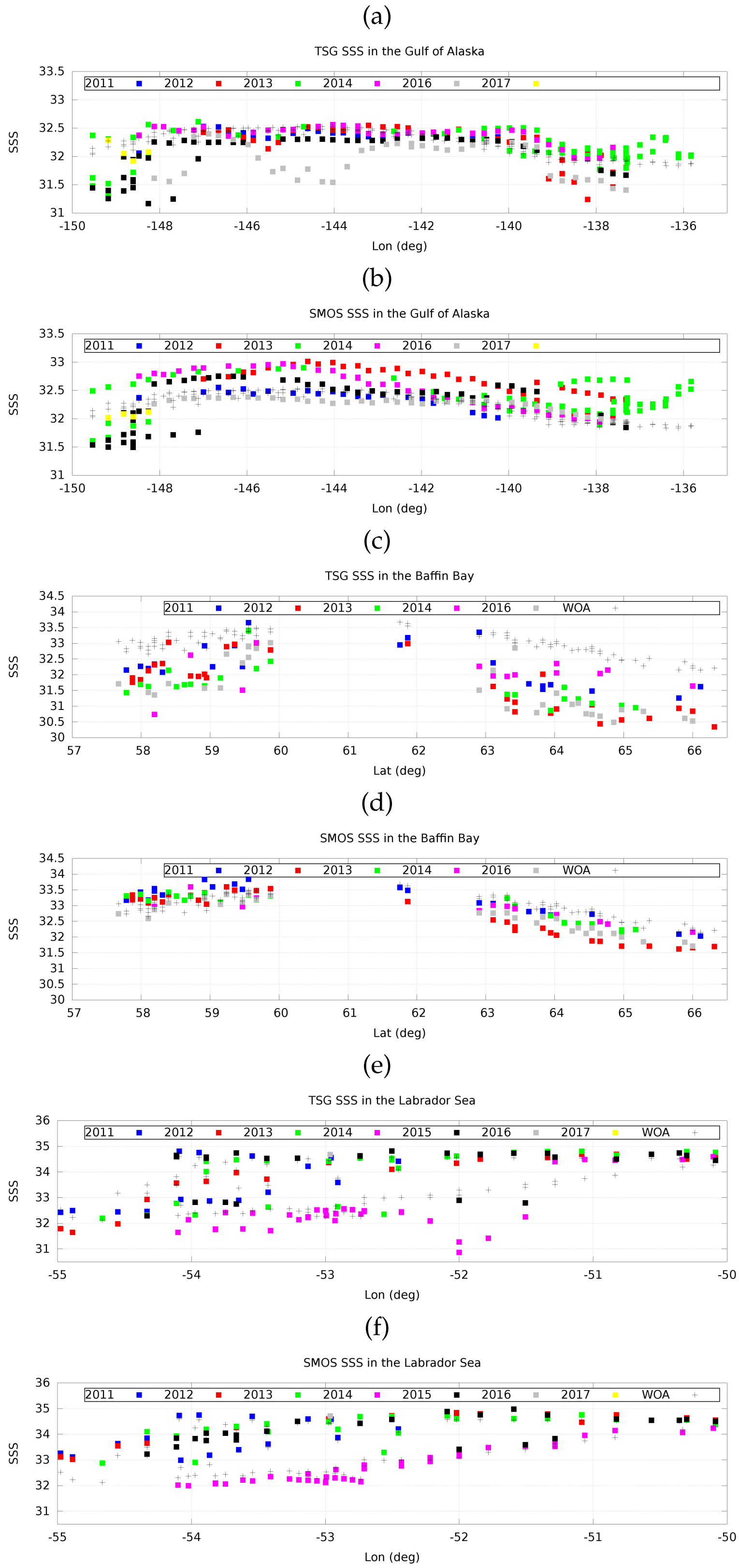

Figure 9. Routinely performed transects during 2011–2017 in: (i) the Gulf of Alaska as observed by TSG ((**a**) plot) and SMOS ((**b**) plot) in a zonal transect around 58°N and 150°W–135°W; (ii) the Baffin Bay as observed by TSG ((**c**) plot) and SMOS ((**d**) plot) in a meridional transect around 79°W and 57°N–67°N; and the Labrador Sea as observed by TSG ((**e**) plot) and SMOS ((f) plot) in a diagonal transect in the range of latitudes from 50°N to 60°N and in the longitude range from 55°W to 50°W.

In the central part of the Gulf of Alaska ((a) and (b) plots of Figure 9, longitudes between 146°W and 143°W), TSG captures a fresh anomaly in 2016. The freshest year measured by SMOS in this range of longitudes is also 2016, although SMOS does not capture the sudden freshening. The inter-annual variability captured in the eastern part of the gulf (longitudes between 137°W and 135°W) for 2013 and 2015 (green and black points, respectively) is also coherent between both sources: both SMOS and TSG show 2013 being saltier than 2015.

Close to the coast of Baffin Island ((c) and (d) plots of Figure 9, latitudes between 63°N and 65°N), the two freshest years as observed by TSG are 2012 and 2016 (red and grey points). These are also the two freshest years captured by SMOS. On the coast of Canada (latitudes between 57°N and 60°N), TSG captures a large fresh anomaly in 2014. In this case, SMOS does not capture the freshening. The (c) plot of Figure 9 shows that, in the range of 58.25°N–58.75°N, consecutive pink points jump from 30.5 to 32.5. This strong SSS gradient occurs over a very short distance, which is smaller than the correlation radii used in the objectively analyzed SMOS SSS fields. Therefore, this SMOS SSS product cannot capture this gradient. In the Labrador Sea ((e) and (f) plots of Figure 9), both SSS sources agree on the fact that the 2014 (pink pixels) is the freshest one.

Figure 10 shows the scatter plots of SMOS SSS and TSG SSS (red) and WOA and TSG SSS (blue), for the three previous cases of study. To better illustrate the added value of SMOS with respect to the selected annual reference (WOA), several statistical parameters (number of points, linear regression coefficient, RMS of the regression residuals and Pearson correlation) as well as the corresponding linear regression lines are also shown. In all three regions, the SMOS SSS data are in better agreement with TSG than the WOA SSS, as shown by the different statistical parameters. This is notably the case for both the Gulf of Alaska and the Baffin Bay regions, where the SMOS SSS correlations are, respectively, 0.73 and 0.79, while those of the WOA are 0.42 and 0.68. Moreover, the SMOS SSS regression lines (red lines) are closer to the diagonal than those from the WOA data set (blue lines). In the Labrador Sea the added value of SMOS SSS with respect to WOA is less pronounced.

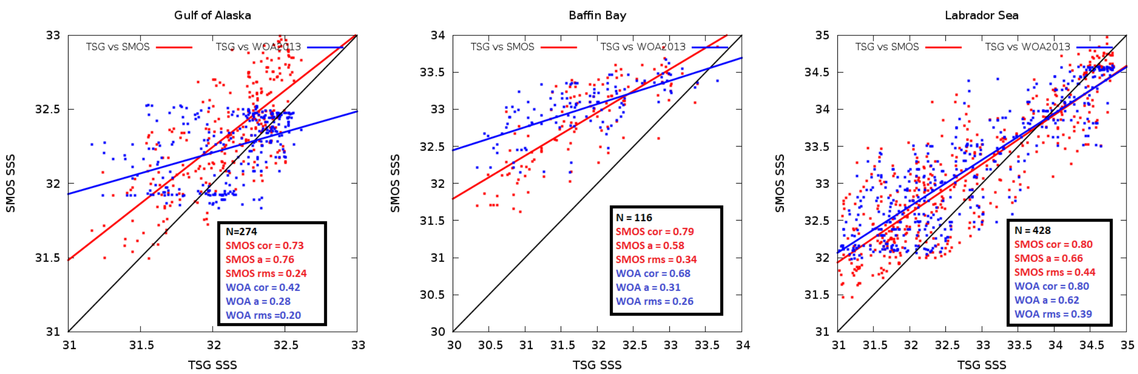

Figure 10. Correlation between SMOS SSS and TSG SSS in the three transects presented in Figure 9: Gulf of Alaska (**left**); Baffin Bay (in the **middle**); and Labrador Sea (**right**). Red line is the linear regression between SMOS SSS and TSG SSS (red points) and blue line is the linear regression between WOA SSS and TSG SSS (blue points). The number of measurements (N), the correlation coefficient (cor), the coefficient of linear regression (a) and the RMS of the residuals are shown in the legend for SMOS SSS (red) and WOA SSS (blue).

5. Sea Surface Salinity Variability Observed by SMOS at the Mouth of the Main Arctic Rivers

The largest intra-annual variability observed by SMOS is located near the mouth of the main Arctic rivers. In Section 4.3, we show that the inter annual variations of SSS described by SMOS agree with the ones described by TSG SSS in sub-Arctic regions. However, inside the Arctic basin, very few in situ measurements are available. In this section, we show that SMOS SSS variability is consistent with the SSS dynamics of the region, in the Arctic basin. In particular, we analyze the SSS variability close to the mouth of the Mackenzie and Ob Rivers. We compare the SMOS SSS maps with the output of the TOPAZ model and with the remotely sensed SSS provided by Aquarius and SMAP. We also look at the discharge data provided by Arctic Great Rivers project to correlate the freshening observed by SMOS to the river discharge events.

In Figure 11, monthly SMOS SSS maps (July, August and September) close to the mouth of the Mackenzie and Ob Rivers are shown (left and right plots, respectively). In Figure 12, TOPAZ SSS maps are displayed for the same months and regions. In Figure 13, the same regions and months are also used for representing Aquarius SSS maps (for years 2012 and 2014) and SMAP SSS maps (for years 2016 and 2017 in the case of the maps close to the Mackenzie River and 2015 and 2017 in the case of the maps close to the Ob River). Ice mask thresholds are different: the SMAP products use the limit of 3% of Sea Ice Concentration (SIC) computed with the Bootstrap algorithm [52], above this threshold that pixel is not considered water and is filtered out; Aquarius uses a threshold of 15% of the same algorithm; SMOS considers water pixels those with a SIC lower than 15% by using the EUMETSAT Ocean and Sea Ice Satellite application Facility (OSI-SAF) product.

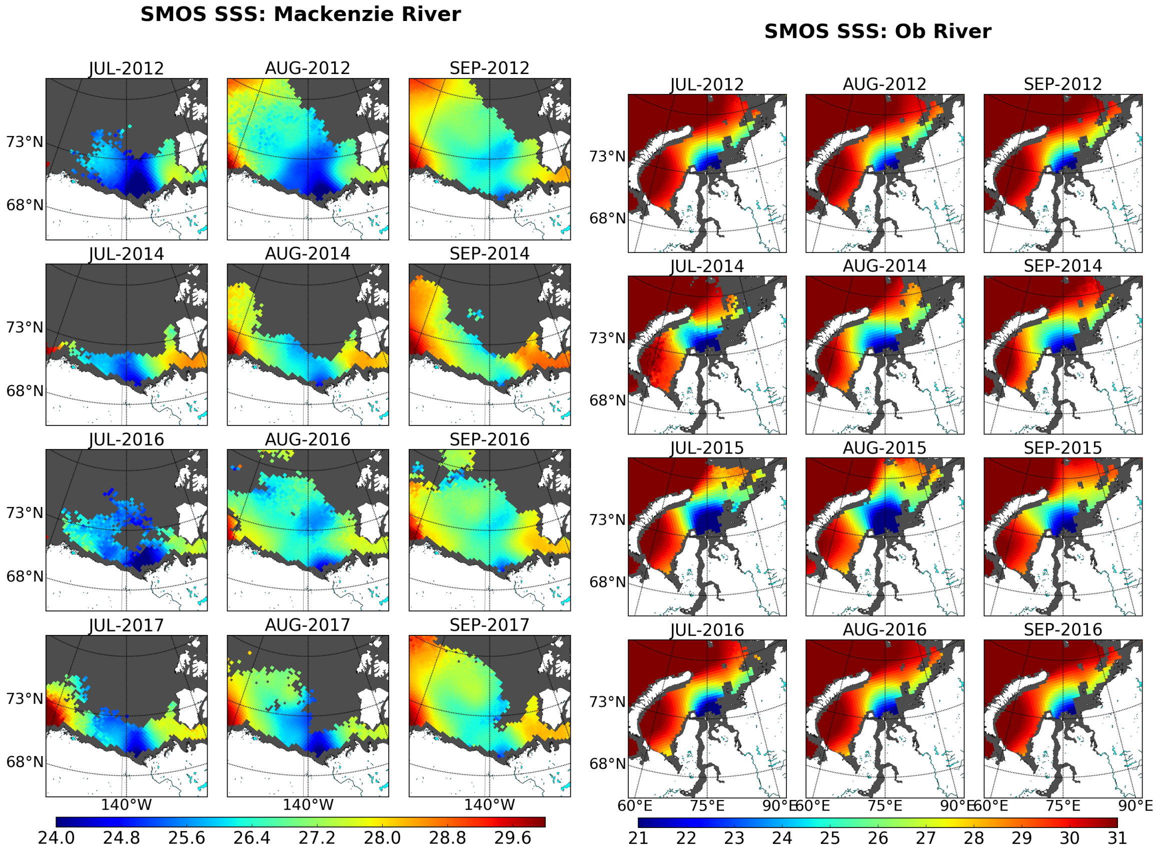

Figure 11. Monthly SMOS SSS maps close to the mouth of Mackenzie River: (**left**); and Ob River (**right**).

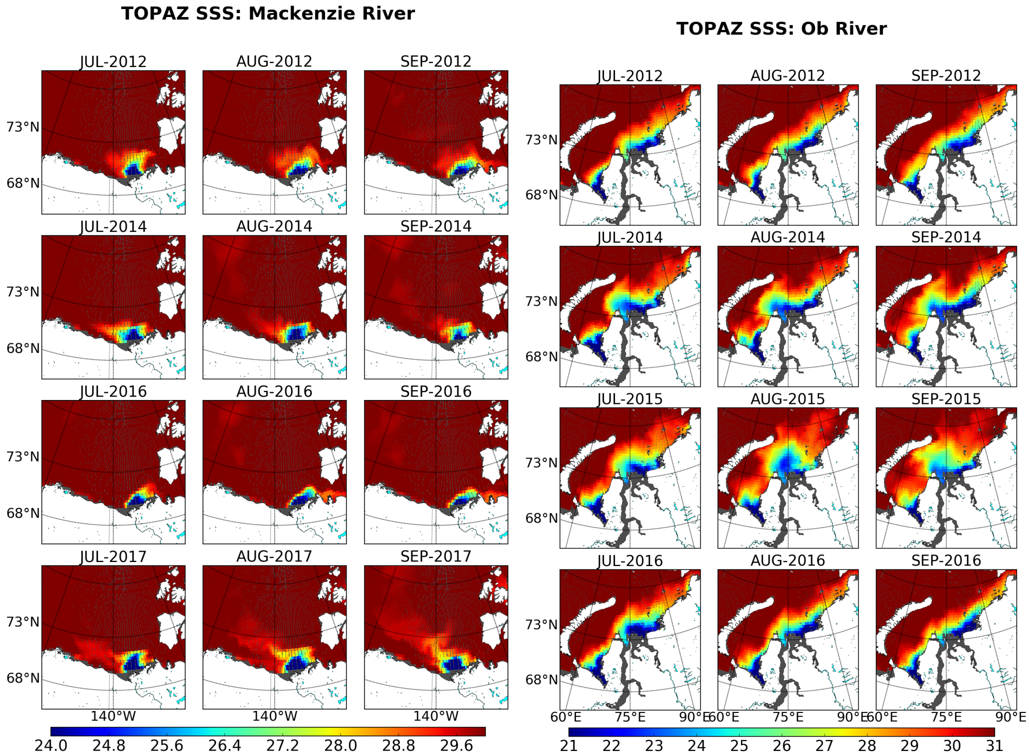

Figure 12. Monthly TOPAZ SSS maps close to the mouth of Mackenzie River: (**left**); and Ob River (**right**).

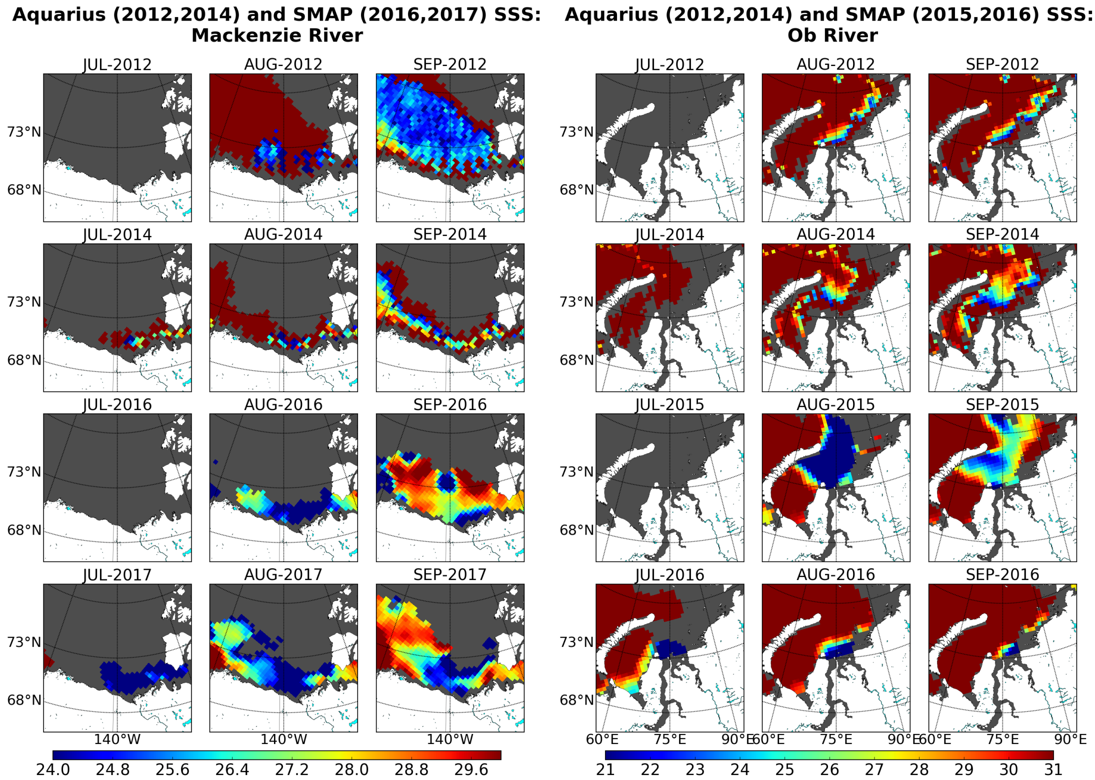

Figure 13. Monthly Aquarius and SMAP SSS maps close to the mouth of: Mackenzie River (**left**); and Ob River (**right**).

Figure 14 shows the daily river discharge of the Mackenzie and Ob Rivers. The Mackenzie River presents the maximum discharge by the end of May, except in 2012 when two maximums were observed (Figure 14 left). At that time, there is still a high percentage of sea ice in the region. Sea ice can be considered melted (less than 30% of ice concentration) by mid-July, except for 2013, when it melted slightly later (not shown). Due to the strong density stratification of the Arctic Ocean, the newly supplied fresh water tends to stay at the surface in the absence of enough strong wind-driven stirring. The persistence of the river plume on surface is well observed in the temporal evolution (July–August) of SMOS SSS maps in the Mackenzie River (left plots of Figure 11). The output SSS from the TOPAZ model in the mouth of the Mackenzie River (left plots of Figure 12) shows a smaller plume than the one displayed by SMOS. It does not change noticeably during the different years, while SMOS shows important inter annual differences. Moreover, variability for different months is not observed with TOPAZ outputs, while it is observed very clearly with SMOS. Aquarius SSS (2012 and 2014 of the left plots of Figure 13) suffers from strong positive biases with respect to the SSS captured by SMOS and TOPAZ at the ice edge. Although the ice mask in SMAP is more restrictive than for SMOS, both satellites observe coherent plumes structures. However, SMAP SSS gradients are larger than the ones captured by SMOS.

Daily river discharge data illustrates that the maximum discharge of the Ob River occurs by the end of May (in Figure 14 right), and that the greatest discharge happened in 2015. Since the region is almost melted around the beginning of July, the maximum Ob River discharge occurs before the sea water is free of ice.

Despite of the differences in the grid resolution: 12.5 km for TOPAZ and 25 km for SMOS, the plume of the Ob River described by TOPAZ (right plots of Figure 12) seems more consistent with the one described by SMOS (right plots of Figure 11) than in the case of the Mackenzie plume (in terms of SSS variability and the spatial coverage of the plume). Aquarius maps (right plots of Figure 13) display saltier SSS than SMOS, SMAP and TOPAZ close to the Ob River mouth, which does not seem geophysically reasonable. The inter annual variations shown by SMAP and SMOS (right plots of Figures 11 and 13) are also coherent. For example, 2015 is the year that both satellites display the major extension of fresh water in July and August, even though SMAP shows a larger plume than SMOS. This is also coherent with the in situ river discharge data shown in Figure 14 (right). TOPAZ maps also show a large extension of fresh water in 2015.

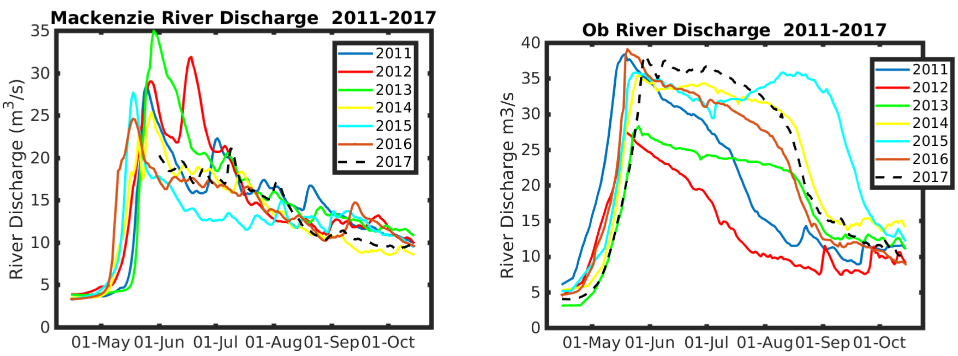

Figure 14. Daily river discharge from 2011 to 2017 from Arctic Great Rivers project: Mackenzie River (**left**); and Ob River (**right**).

In Figure 15, we compare monthly SMOS SSS anomalies with respect to monthly river discharge anomalies. These anomalies are computed as follows. First, the daily river discharge data are monthly averaged. Since these regions are frozen in winter months, and we are interested in comparing these data with SSS, we consider as reference the average of the monthly discharge of June, July, August and September for the seven years of study (2011–2017). The monthly discharge anomalies (green points in Figure 15) are generated by subtracting this reference to the monthly discharge data. Consistently, we consider as SMOS SSS reference the average of the monthly SMOS SSS maps of June, July, August and September for 2011–2017. The SMOS SSS anomalies shown in Figure 15 are the differences between the monthly SMOS SSS maps and the mentioned reference. The purple points represent the spatial average of these SMOS SSS anomalies in two regions close to the mouth of the Mackenzie River (latitudes between 69°N and 73°N and longitudes between 150°W and 130°W) and the Ob River (latitudes between 73°N and 77°N and longitudes between 60°E and 90°E). The relationship between the SSS anomaly and the discharge anomaly is not straightforward. The geophysical phenomena that play a role on the modification of the SSS in those regions are diverse and complex, for example the melting of the ice, the mixing due to wind, water advection, etc. A complete understanding of the interactions of these phenomena and the salinity are out of the scope of this work. At this stage, a more qualitative analysis is carried out, i.e., to check whether decreasing trends of SMOS SSS anomalies are linked to positive trends of river discharge anomalies and vice versa. As already mentioned, in both cases (Mackenzie and Ob Rivers), the maximum discharge happens in May when the region is usually frozen. That is why the green lines in Figure 15 usually show a decreasing trend. Consequently, increasing trends of SMOS SSS anomalies (purple lines) are expected. Figure 15 shows that, typically, SMOS SSS anomalies increase from July. However, from June to July, both the SMOS SSS and river discharge anomalies mainly show a decreasing trend. This can be explained by several mechanisms: on the one hand, the discharge measurements are not performed in the mouth of the rivers, therefore a delay between the discharge variations and the SSS response is expected, while, on the other hand, as already discussed, these regions are typically strongly stratified and, when the wind is not strong enough, the newly supplied fresh water tends to stay at the surface. Additionally, in July, the ice melting still occurs and refreshes the water in those regions. For the rest of months, an anti-symmetric (anti-correlated) behavior of the SSS with respect to the river discharge is observed (as expected).

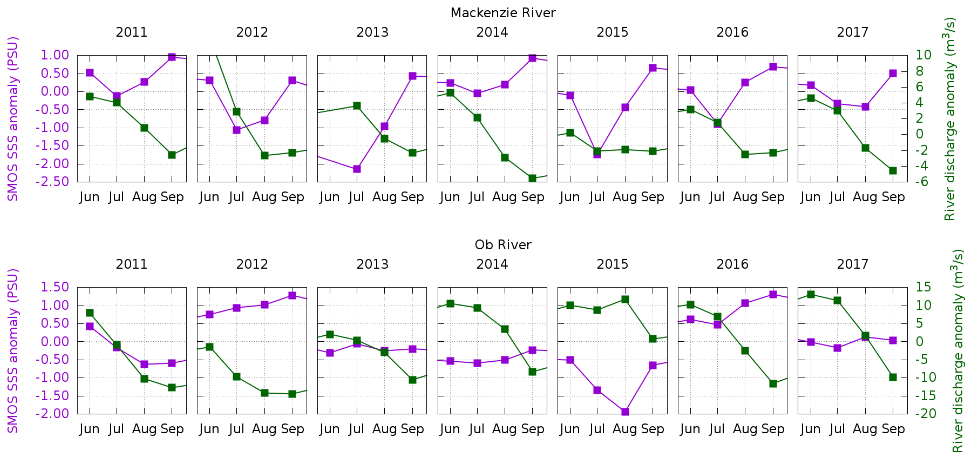

Figure 15. Monthly SMOS SSS anomaly (purple) versus monthly river discharge anomaly (green) from 2011 to 2017 from Arctic Great Rivers project: Mackenzie River (**top**); and Ob River (**bottom**).

6. Conclusions

This paper demonstrates the capability of SMOS-derived SSS to follow the vast salinity spatial and temporal variability in Arctic and sub-Arctic regions. This new product is produced using the retrieval algorithm proposed by Olmedo et al. [23] and includes some improvements with respect to the initial data set distributed by the Barcelona Expert Center. In particular, an enhanced time-dependent bias correction is applied. We also analyze the impact of considering different annual SSS references for the generation of the product. The conclusion of this analysis is that there are regions in the Arctic Ocean where the analyzed references are of poor quality, and, therefore, the corresponding SMOS SSS products suffer from spatial biases (which are constant in time). However, the dynamical range of the SSS described by these annual references (and also by the SMOS product) is geophysically consistent. Additionally, we analyze which is the most appropriate correlation radii for the generation of the objectively analyzed SSS fields. The conclusion of this analysis is that correlation radii greater than what is expected by the dynamics of the region provide the lowest error with respect to Argo floats, probably because the SMOS SSS retrievals have a larger error than in other regions (of warmer waters).

Validation of SMOS salinity maps at high latitudes against Argo floats shows that the product has a std in the range of 0.24–0.35. We have also used a dataset of 86 TSG provided by Copernicus. Besides the statistics of the differences between SMOS and TSG, we analyze the inter annual variations described by each one of the two SSS sources. SMOS and TSG SSS are in agreement in the major features of the SSS dynamics, although, as expected, the spatial scales that are resolved by SMOS are blurred with respect to the ones resolved by the TSG. It is important to notice that most of the measurements used in these comparisons are located outside the Arctic Ocean. Therefore, this comparison cannot be used to project a realistic quality assessment of SMOS SSS maps inside the Arctic Circle.

To complete the overview of the quality of this SMOS SSS product in the Arctic regions, we compare the SMOS SSS with TOPAZ, Aquarius and SMAP SSS close to two of the main rivers of the Arctic Ocean: the Mackenzie and Ob Rivers. We observe that the output from TOPAZ underestimates the plume of the Mackenzie River. Aquarius SSS maps are probably affected by ice–sea (and maybe also by some residual land–sea) contamination, showing saltier waters than the other satellite datasets do. Despite the differences in the ice mask, the inter- and intra-annual variations described by SMAP and SMOS are quite consistent. Although a more extensive work on the comparison between the remote sensed salinity products is still required, these results suggest that both SMOS and SMAP have great potential to routinely monitor the extension of the surface freshwater fluxes in the Arctic Ocean.

Even though the original resolution of the SMOS SSS is $\approx$40 km, the selected correlation radii are likely too large to monitor some mesoscale features of these Arctic and sub-Arctic regions. The reduction of the correlation radii will be driven by the reduction of the noise of the salinity retrievals. Future improvements of this SMOS SSS product are aimed at reducing the error of the salinity retrievals at high latitudes. Enhanced image reconstruction techniques as the one introduced in [48] have been assessed in [49,50] reaching promising results. The decrease of the error in the salinity retrieval would allow generating SMOS SSS maps with smaller correlation radii. Then, a richer mesoscale dynamics is expected to be captured by the future SMOS SSS products.

Finally, we would like to underline the need of implementing more in situ measurements in Arctic regions. On the one hand, they are absolutely required for a proper assessment of the satellite products in these regions. On the other hand, they are also required for the computation of a better annual reference in the Arctic Ocean. There are still many regions in the Arctic Ocean where very few measurements have been used for the computation of the salinity climatology. This in particular means that the knowledge of the salinity of those regions is really limited.

Author Contributions: Estrella Olmedo and Carolina Gabarró conceived and designed the idea of the manuscript. Estrella Olmedo conceived and implemented the algorithm for the SMOS SSS products generation. Estrella Olmedo and Carolina Gabarró performed the validation of the new SMOS SSS product. The manuscript was prepared by Estrella Olmedo and Carolina Gabarró. All authors contributed to the scientific discussions, revised and approved the final manuscript.

Funding: This research was funded by the Spanish R+D plan under projects L-BAND (ESP2017-89463-C3-1-R) and PROMISES (ESP2015-67549-C3-2) and from European Space Agency by means of the contracts SMOS ESL L2OS, CCI+ SSS and Arctic+ SSS.

Acknowledgments: This work was supported by the Spanish R+D plan under projects L-BAND (ESP2017-89463-C3-1-R) and PROMISES (ESP2015-67549-C3-2) and from European Space Agency by means of the contracts SMOS ESL L2OS, CCI+ SSS and Arctic+ SSS. We would like to thanks James McClelland, for offering us the daily river discharge data. We acknowledge Copernicus and Met Office Hadley Centre for providing TOPAZ and ESA for the L1B SMOS dataset. The authors would also like to thank LOCEAN for providing the Arctic TARA campaign dataset. Argo data were collected and made freely available by the International Argo Program and the national programs that contribute to it (http://www.argo.ucsd.edu,http://argo.jcommops.org). The Argo Program is part of the Global Ocean Observing System. The authors are grateful to the anonymous reviewers for their helpful suggestions.

Conflicts of Interest: The authors declare no conflict of interest.

References

1. Serreze, M.C.; Holland, M.M.; Stroeve, J. Perspectives on theArctic's shrinking sea-ice cover. *Science* **2007**, *315*, 1533–1536. [CrossRef] [PubMed]
2. Haas, C.; Pfaffling, A.; Hendricks, S.; Rabenstein, L.; Etienne, J.L.; Rigor, I. Reduced ice thickness in Arctic transpolar drift favors rapid ice retreat. *Geophys. Res. Lett.* **2008**, *35*. [CrossRef]
3. Comiso, J.C. Large Decadal Decline of the Arctic Multiyear Ice Cover. *J. Clim.* **2012**, *25*, 1176–1193. [CrossRef]
4. Haine, T.; Curry, B.; Gerdes, R.; Hansen, E.; Karcher, M.; Lee, C.; Rudels, B.; Spreen, G.; de Steur, L.; Stewart, K.D.; et al. Arctic freshwater export: Status, mechanisms, and prospects. *Glob. Planet. Chang.* **2015**, *125*, 13–35. [CrossRef]
5. Zhang, J.; Steele, M.; Runciman, K.; Dewey, S.; Morison, J.; Lee, C.; Rainville, L.; Cole, S.; Krishfield, R.; Timmermans, M.L.; et al. The Beaufort Gyre intensification and stabilization: A model-observation synthesis. *J. Geophys. Res. Oceans* **2016**. [CrossRef]
6. Rabe, B.; Karcher, M.; Kauker, F.; Schauer, U.; Toole, J.M.; Krishfield, R.A.; Pisarev, S.; Kikuchi, T.; Su, J. Arctic Ocean basin liquid freshwater storage trend 1992–2012. *Geophys. Res. Lett.* **2014**, *41*, 961–968. [CrossRef]
7. Peterson, B.; Holmes, R.; McClelland, J.; Vörösmarty, C.; Lammers, R.; Shiklomanov, A.; Shiklomanov, I.; Rahmstorf, S. Increasing river discharge to the Arctic Ocean. *Science* **2002**, *298*, 2171–2173. [CrossRef] [PubMed]
8. Mulligan, R.P.; Perrie, W.; Solomon, S. Dynamics of the Mackenzie River plume on the inner Beaufort shelf during an open water period in summer. *Estuar. Coast. Shelf Sci.* **2010**, *89*, 214–220. [CrossRef]
9. Jeffries, M.; Richter-Menge, J.; Overland, J.E. Arctic Report Card 2015. Technical Report, NOAA Reports. Available online: https://www.arctic.noaa.gov/Report-Card (accessed on 8 November 2018).
10. Font, J.; Camps, A.; Ballabrera-Poy, J. *'Microwave Aperture Synthesis radiometry: Setting the Path for Sea Surface Salinity Measurements from Space' in Remote Sensing of European Seas*; Springer: Berlin, Germany, 2008; ISBN 978-1-4020-6771-6.
11. Mecklenburg, S.; Wright, N.; Bouzina, C.; Delwart, S. Getting down to business—SMOS operations and products. *ESA Bull.* **2009**, *137*, 25–30.
12. Kerr, Y.; Waldteufel, P.; Wigneron, J.; Delwart, S.; Cabot, F.; Boutin, J.; Escorihuela, M.; Font, J.; Reul, N.; Gruhier, C.; et al. The SMOS mission: New tool for monitoring key elements of the global water cycle. *Proc. IEEE* **2010**, *98*, 666–687. [CrossRef]
13. Le Vine, D.; Lagerloef, G.; Colomb, F.; Yeh, S.; Pellerano, F. Aquarius: an instrument to monitor sea surface salinity from space. *IEEE Trans. Geosci. Remote Sens.* **2007**, *45*, 2040–2050. [CrossRef]
14. Lagerloef, G.; Colomb, F.; LeVine, D.; Wentz, F.; Yueh, S.; Ruf, C.; Lilly, J.; Gunn, J.; Chao, Y.; de Charon, A.; et al. The Aquarius/Sac-D mission: designed to meet the salinity remote-sensing challenge. *Oceanography* **2008**, *21*, 68–81. [CrossRef]
15. Entekhabi, D.; Njoku, E.; O'Neill, P.; Kellogg, K.; Crow, W.; Edelstein, W.; Entin, J.; Goodman, S.; Jackson, T.; Johnson, J.; et al. The Soil Moisture Active Passive (SMAP) mission. *Proc. IEEE* **2010**, *98*, 704–716. [CrossRef]
16. Zine, S.; Boutin, J.; Font, J.; Reul, N.; Waldteufel, P.; Gabarro, C.; Tenerelli, J.; Petitcolin, F.; Vergely, J.; Talone, M.; et al. Overview of the SMOS Sea Surface Salinity Prototype Processor. *IEEE Trans. Geosci. Remote Sens.* **2008**, *46*, 621–645. [CrossRef]
17. Swift, C.; McIntosh, R. Considerations for Microwave Remote Sensing of Ocean-Surface salinity. *IEEE Trans. Geosci. Electron.* **1983**, *GE-21*, 480–491. [CrossRef]
18. Yueh, S.; West, R.; Wilson, W.; Li, F.; Nghiem, S.; Rahmat-Samii, Y. Error Sources and Feasibility for Microwave Remote Sensing of Ocean Surface Salinity. *IEEE Trans. Geosci. Remote Sens.* **2001**, *39*, 1049–1059. [CrossRef]
19. Martín-Neira, M.; Oliva, R.; Corbella, I.; Torres, F.; Duffo, N.; Duran, I.; Kainulainen, J.; Closa, A.; Zurita, A.; Cabot, F.; et al. SMOS Instrument performance and calibration after six years in orbit. *Remote Sens. Environ.* **2016**, *180*, 19–39. [CrossRef]
20. Köhler, J.; Sena Martins, M.; Serra, N.; Stammer, D. Quality assessment of spaceborne sea surface salinity observations over the northern North Atlantic. *J. Geophys. Res. Oceans* **2015**, *120*, 94–112. [CrossRef]
21. Matsuoka, A.; Babin, M.; Devred, E. A new algorithm for discriminating water sources from space: A case study for the southern Beaufort Sea using MODIS ocean color and SMOS salinity data. *Remote Sens. Environ.* **2016**, *184*, 124–138. [CrossRef]

22. Tang, W.; Yueh, S.; Yang, D.; Fore, A.; Hayashi, A.; Lee, T.; Fournier, S.; Holt, B. The Potential and Challenges of Using Soil Moisture Active Passive (SMAP) Sea Surface Salinity to Monitor Arctic Ocean Freshwater Changes. *Remote Sens.* **2018**, *10*. [CrossRef]
23. Olmedo, E.; Martinez, J.; Turiel, A.; Ballabrera-Poy, J.; Portabella, M. Debiased non-Bayesian retrieval: A novel approach to SMOS Sea Surface Salinity. *Remote Sens. Environ.* **2017**, *193*, 103–126. [CrossRef]
24. Isern-Fontanet, J.; Olmedo, E.; Turiel, A.; Ballabrera-Poy, J.; García–Ladona, E. Retrieval of eddy dynamics from SMOS sea surface salinity measurements in the Algerian Basin (Mediterranean Sea). *Geophys. Res. Lett.* **2016**, *43*, 6427–6434. [CrossRef]
25. Olmedo, E.; Taupier-Letage, I.; Turiel, A.; Alvera-Azcárate, A. Improving SMOS Sea Surface Salinity in the Western Mediterranean Sea through Multivariate and Multifractal Analysis. *Remote Sens.* **2018**, *10*. [CrossRef]
26. Garcia-Eidell, C.; Comiso, J.; Dinnat, E.; Brucker, L. Satellite observed salinity distributions at high latitudes in the Northern Hemisphere: A comparison of four products. *J. Geophys. Res. Ocean* **2017**, *122*, 7717–7736. [CrossRef]
27. Argo. Argo float data and metadata from Global Data Assembly Centre (Argo GDAC). *SEANOE* **2000**. [CrossRef]
28. Reverdin, G.; Le Goff, H.; Tara Oceans Consortium, Coordinators; Tara Oceans Expedition, Participants. Properties of seawater from a Sea-Bird TSG temperature and conductivity sensor mounted on the continuous surface water sampling system during campaign TARA_20090913Z of the Tara Oceans expedition 2009–2013. *PANGAEA* **2014**. . [CrossRef]
29. Chassignet, E.P.; Hurlburt, H.E.; Metzger, E.J.; Smedstad, O.M.; Cummings, J.; Halliwell, G.R.; Bleck, R.; Baraille, R.; Wallcraft, A.; Lozano, C.; et al. Global Ocean Prediction with the HYbrid Coordinate Ocean Model (HYCOM). *Oceanography* **2009**, *22*, 64–75. [CrossRef]
30. Sakov, P.; Counillon, F.; Bertino, L.; Lisæter, K.A.; Oke, P.R.; Korablev, A. TOPAZ4: An ocean-sea ice data assimilation system for the North Atlantic and Arctic. *Ocean Sci.* **2012**, *8*, 633–656. [CrossRef]
31. Korosov, A.; Counillon, F.; Johannessen, A. Monitoring the spreading of the Amazon freshwater plume by MODIS, SMOS, Aquarius and TOPAZ. *J. Geophys. Res. Oceans* **2015**, *120*, 268–283. [CrossRef]
32. Brucker, L.; Dinnat, E.; Koenig, L. *Aquarius L3 Weekly Polar-Gridded Sea Surface Salinity, Version 6*; NASA National Snow and Ice Data Center Distributed Active Archive Center: Boulder, CO, USA, 2015. [CrossRef]
33. Brodzik, M.J.; Billingsley, B.; Haran, T.; Raup, B.; Savoie, M.H. EASE-Grid 2.0: Incremental but Significant Improvements for Earth-Gridded Datasets. *ISPRS Int. J. Geo-Inf.* **2012**, *1*, 32–45. [CrossRef]
34. Fore, A.G.; Yueh, S.H.; Tang, W.; Stiles, B.W.; Hayashi, A.K. Combined Active/Passive Retrievals of Ocean Vector Wind and Sea Surface Salinity With SMAP. *IEEE Trans. Geosci. Remote Sens.* **2016**, *54*, 7396–7404. [CrossRef]
35. Tenerelli, J.; Reul, N.; Mouche, A.; Chapron, B. Earth-Viewing L-Band Radiometer Sensing of Sea Surface Scattered Celestial Sky Radiation—Part I: General Characteristics. *IEEE Trans. Geosci. Remote Sens.* **2008**, *46*, 659–674. [CrossRef]
36. Reul, N.; Tenerelli, J.; Guimbard, S.; Collard, F.; Kerbaol, V.; Skou, N.; Cardellach, E.; Tauriainen, S.; Bouzinac, C.; Wursteisen, P.; et al. Analysis of L-band radiometric measurements conducted over the North Sea during the CoSMOS-OS airborne campaign. In Proceedings of the IEEE International Geoscience and Remote Sensing Symposium (IGARSS2007), Barcelona, Spain, 23–27 July 2007.
37. Guimbard, S.; Gourrion, J.; Portabella, M.; Turiel, A.; Gabarro, C.; Font, J. SMOS Semi-Empirical Ocean Forward Model Adjustment. *IEEE Trans. Geosci. Remote Sens.* **2012**, *50*, 1676–1687. [CrossRef]
38. Sabater, J.; De Rosnay, P. *Tech Note—Parts 1/2/3: Operational Pre-processing Chain, Collocation Software Development and Offline Monitoring Suite*; Technical Report; ECMWF: Reading, Uk, 2010.
39. Meissner, T.; Wentz, F. The complex dielectric constant of pure and sea water from microwave satellite observations. *IEEE Trans. Geosci. Remote Sens.* **2004**, *42*, 1836–1849. [CrossRef]
40. Klein, L.; Swift, C. An Improved Model for the Dielectric Constant of Sea Water at Microwave Frequencies. *IEEE Trans. Antennas Propag.* **1977**, *AP-25*, 104–111. [CrossRef]
41. Dinnat, E.P.; Boutin, J.; Yin, X.; Vine, D.M.L. Inter-comparison of SMOS and Aquarius Sea Surface Salinity: Effects of the dielectric constant and vicarious calibration. In Proceedings of the 2014 13th Specialist Meeting on Microwave Radiometry and Remote Sensing of the Environment (MicroRad), Pasadena, CA, USA, 24–27 March 2014; pp. 55–60. [CrossRef]

42. Brodzik, M.J.; Knowles, K.W. EASE-Grid: A Versatile Set of Equal-Area Projections and Grids. In *Discrete Global Grids*; National Center for Geographic Information & Analysis: Santa Barbara, CA, USA, 2002.
43. Gabarro, C.; Portabella, M.; Talone, M.; Font, J. Toward an Optimal SMOS Ocean Salinity Inversion Algorithm. *IEEE Geosci. Remote Sens. Lett.* **2009**, *6*, 509–513. [CrossRef]
44. Tenerelli, J.; Reul, N. *Analysis of L1PP Calibration Approach Impacts in SMOS Tbs and 3-Days SSS Retrievals over the Pacific Using an Alternative Ocean Target Transformation Applied to L1OP Data*; Technical Report; IFREMER/CLS: Paris, France, 2010.
45. Zweng, M.; Reagan, J.; Antonov, J.; Locarnini, R.; Mishonov, A.; Boyer, T.; Garcia, H.; Baranova, O.; Johnson, D.; Seidov, D.; et al. *World Ocean Atlas 2013, Volume 2: Salinity*; A. Mishonov Technical, Levitus, Eds.; NOAA Atlas NESDIS 74; NOAA: Washington, DC, USA, 2013; p. 39.
46. Steele, M.; Morley, R.; Ermold, W. PHC: A global ocean hydrography with a high-quality Arctic Ocean. *J. Clim.* **2001**, *9*, 2079–2087. [CrossRef]
47. Nurser, A.; Bacon, S. The Rossby radius in the Arctic Ocean. *Ocean Sci.* **2014**, *10*, 967–975. [CrossRef]
48. González-Gambau, V.; Turiel, A.; Olmedo, E.; Martínez, J.; Corbella, I.; Camps, A. Nodal Sampling: A New Image Reconstruction Algorithm for SMOS. *IEEE Trans. Geosci. Remote Sens.* **2016**, *54*, 2314–2328. [CrossRef]
49. González-Gambau, V.; Olmedo, E.; Turiel, A.; Martínez, J.; Ballabrera-Poy, J.; Portabella, M.; Piles, M. Enhancing SMOS brightness temperatures over the ocean using the nodal sampling image reconstruction technique. *Remote Sens. Environ.* **2016**, *180*, 202–220. [CrossRef]
50. González-Gambau, V.; Olmedo, E.; Martínez, J.; Turiel, A.; Duran, I. Improvements on Calibration and Image Reconstruction of SMOS for Salinity Retrievals in Coastal Regions. *IEEE J. Sel. Top. Appl. Earth Obs. Remote Sens.* **2017**, *10*, 3064–3078. [CrossRef]
51. Boutin, J.; Chao, Y.; Asher, W.E.; Delcroix, T.; Drucker, R.; Drushka, K.; Kolodziejczyk, N.; Lee, T.; Reul, N.; Reverdin, G.; et al. Satellite and In Situ Salinity: Understanding Near-Surface Stratification and Subfootprint Variability. *Bull. Am. Meteorol. Soc.* **2016**, *97*, 1391–1407. [CrossRef]
52. Comiso, J.C.; Meier, W.N.; Gersten, R. Variability and trends in the Arctic Sea ice cover: Results from different techniques. *J. Geophys. Res. Oceans* **2017**, *122*, 6883–6900. [CrossRef]